Selective Methanol-to-Formate Electrocatalytic Conversion on Branched Nickel Carbide

Junshan Li, Ruilin Wei, Xiang Wang, Yong Zuo, Xu Han, Jordi Arbiol, Jordi Llorca, Yaoyue Yang, Andreu Cabot, Chunhua Cui

Abstract. A methanol economy will be favored by the availability of low-cost catalysts able to selectively oxidize methanol to formate. This selective oxidation would allow extraction of the largest part of the fuel energy while concurrently producing a chemical with even higher commercial value than the fuel itself. Herein, we present a highly active methanol electrooxidation catalyst based on abundant elements and with an optimized structure to simultaneously maximize interaction with the electrolyte and mobility of charge carriers. In situ infrared spectroscopy combined with nuclear magnetic resonance spectroscopy showed that branched nickel carbide particles are the first catalyst determined to have nearly 100 % electrochemical conversion of methanol to formate without generating detectable CO_2 as a byproduct. Electrochemical kinetics analysis revealed the optimized reaction conditions and the electrode delivered excellent activities. This work provides a straightforward and cost-efficient way for the conversion of organic small molecules and the first direct evidence of a selective formate reaction pathway.

Methanol is not only one of the most used commodity chemicals but also an excellent energy vector. It is characterized by a high energy density (15.6 MJ L^{-1}), several times above that of liquid H_2 (4.7 MJ L^{-1}).[1] Being liquid at ambient temperature and pressure, methanol allows for an easy storing and transportation, and it could be distributed using the already existing infrastructure. Additionally, it can be renewably obtained from biomass, organic waste or CO_2.[2] All of these advantages, provide direct methanol fuel cells (DMFCs) with a high potential to power future electric cars and mobile applications, among other.[3] However, the massive depletion of DMFCs is currently impeded by the lack of active, durable and cost-effective catalysts, particularly for the methanol oxidation reaction (MOR).[4]

MOR is generally considered to proceed through a dual-pathway that involves either CO_{ad} or formate intermediates.[5] In the CO_{ad} path, the over-strong adsorption of CO poisons active catalytic sites limiting the catalyst durability. On the other hand, formate weakly bonds to the catalyst surface and it is easily dissolved in alkaline media. Thus, while the formate path does not allow the complete

methanol oxidation, and therefore has associated lower energy densities (9.2 MJ L^{-1}), it may be preferred over the CO_{ad} path that rapidly blocks catalyst activity. An additional advantage of a selective conversion of methanol to formate is the lack of CO_2 emissions. On top of this, the production of a valuable chemical such as formate is advantageous in itself and it can reduce the overall fuel cost. Formate is actually an indispensable intermediate in the chemical industry due to its numerous applications in fabric dyeing, printing processes and the pharmaceutical industry.[6] Currently, close to one million tons of formic acid are yearly produced from the combination of methanol with CO at 40 atm and 80 °C and the hydrolysis of the resulting methyl formate.[7] Owing to the high energy used in this process and the high demand, the price per metric ton of formate is a fourfold higher than that of methanol.[8, 9] Therefore, the selective oxidation of methanol to formate can be economically profitable if a proper strategy to collect the reaction product was developed.

The MOR mechanism on Ru, Pd and Pt-based electrodes in alkaline and acid electrolytes has been extensively investigated.[5, 10, 11] These catalysts do not provide a selective conversion of methanol-to-formate and are too expensive and rare to empower the methanol economy. Among the several alternative materials proposed to replace noble metals as MOR catalysts, Ni offers the highest cost-effectiveness. A plethora of Ni[12-14] and Ni-based catalysts, including oxides/hydroxides,[15-17] metal alloys,[18-23] phosphides,[24] chalcogenides,[25] and nitrides,[26] have been developed and tested toward MOR. Surprisingly, the nickel carbide, which a priori offers suitable properties as electrocatalysts, for example, stability, electrical conductivity and element abundance, has not been tested toward MOR. On the other hand, while MOR mechanisms have been well-studied in noble metals, in spite of the high potential of Ni-based catalysts, their MOR pathways remain largely unknown.

Here we propose a cost-effective catalyst based on nickel carbide for the selective oxidation of methanol to formate. To demonstrate the MOR mechanism, we applied advanced in situ and *ex-situ* characterization strategies combined with electrochemical kinetics analysis to identify the adsorbed and dissolved intermediates/products as a function of the applied potentials.

Ni_3C particles were produced from the decomposition of nickel(II) acetylacetonate at 240 °C in a solution of octadecene (ODE) and oleylamine (OAm).[27] Experimental details can be found on the supporting information (SI). Figure **1 a** displays a representative transmission electron microscopy (TEM) micrograph of the particles produced using a solvent ratio ODE/OAm=2. Particles produced under these conditions had an average size of 140±20 nm and appeared highly branched with an average branch width of 19±4 nm. When reducing the ODE/OAm ratio to 1, smaller particles, 53±7 nm, with shorter branches but with approximately the same width were produced (Figure S1). X-ray

diffraction (XRD) patterns showed the crystallographic structure of the produced particles ascribe to the rhombohedral Ni_3C_{1-x} phase (JCPDS 01 072 1467, Figure **1 b**).[28] High resolution TEM (HRTEM) characterization confirmed the crystal structure to the Ni_3C hexagonal phase (space group=R3-CH#167) with *a*=*b*=4.5820 Å and *c*=13.0300 Å.

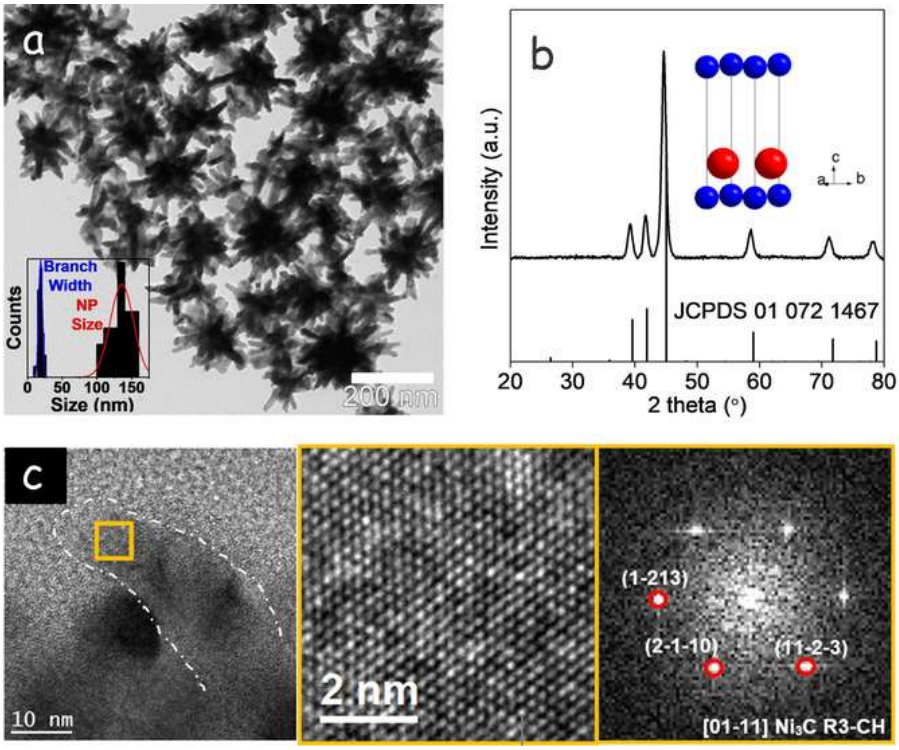

Figure 1. a) Representative TEM image of the particles obtained within a solvent ratio ODE/OAm=2. b) XRD pattern and Ni_3C crystal structure: blue=carbon, red=nickel. c) HRTEM micrograph, detail of the orange squared region and its corresponding power spectrum (FFT).

X-ray photoelectron spectroscopy (XPS) data showed the probed Ni at the Ni_3C surface to have an oxidized $Ni^{2+/3+}$ chemical environment with Ni $2p_{3/2}$ at 857.1 eV (Figure S2).[29] This Ni_3C surface oxidation was attributed to the manipulation of the particles in air atmosphere during purification and transportation.[30, 31]

Thermogravimetric analysis (TGA) of the Ni_3C particles showed a weight loss of a 6.6 wt % when heating the material up to 450 °C (Figure S3). This weight loss was attributed to the desorption of surface water and the decomposition of the surface ligands used to control the NP growth. TGA showed an additional weight loss of a 3.6 wt % at temperature above 500 °C, which was attributed to a carbon release from the structure, in agreement with previous reports.[27] To prepare the catalysts, the organic surface ligands were chemically removed using hydrazine and acetonitrile (see SI for details), and this removal was confirmed by FTIR analysis (Figure S4).

Ni_3C-based electrocatalysts were prepared by drop-casting a solution containing the NPs and carbon black at a 1/2 weight ratio on glassy carbon (see SI for details). Initial cyclic voltammetry (CV) analysis of the electrocatalysts was performed in a 1.0 M KOH electrolyte (Figure **2 a**). During the forward scan, surface Ni was oxidized, first to $Ni(OH)_2$ and later to NiOOH.[19] Ni_3C/C electrodes activated the oxygen evolution reaction (OER) at ca. 0.6–0.7 V vs. Ag/AgCl and the lowest activation potentials were systematically measured with the larger and more branched Ni_3C particles, that is, those produced with ODE/OAm=2.

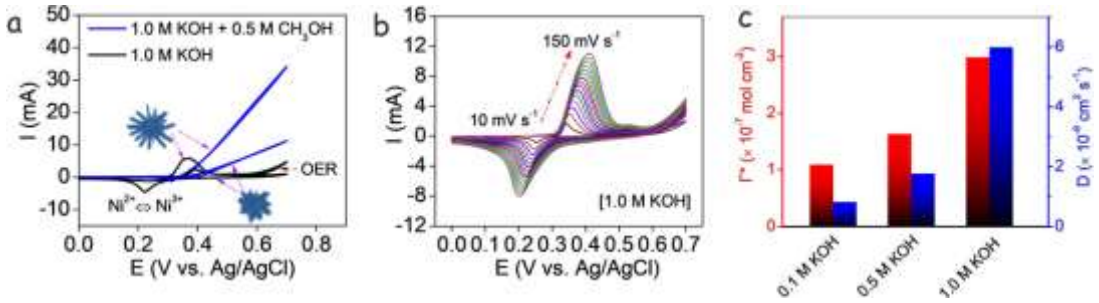

Figure 2. Electrochemical response of Ni_3C-based electrodes in alkaline media. a) CV curves in 1.0 M KOH solution with and without 0.5 M methanol. b) CV curves in 1.0 M KOH at scanning rate from 10 mV s^{-1} to 150 mV s^{-1}. c) Surface coverage of redox species (Γ*) and diffusion coefficient (*D*) obtained in 0.1, 0.5 and 1.0 M KOH solution.

The electrochemically active surface area (ECSA) was estimated from the electrochemical double-layer capacitance (C_{dl}) on the basis of CVs recorded at different scan rates in the non-faradaic potential range 0–0.1 V vs. Ag/AgCl (see Figure S5 and calculations).[32, 33] An ECSA of 6.3 cm^2 was obtained for the largest branched NPs and just 3.8 cm^2 for the smallest ones.

Figures **2 b** and S6ab display CVs with a stepwise increase of scanning rates from 10 to 150 mV s^{-1} in 1.0 M, 0.5 M and 0.1 M KOH. At the same scan rate of 50 mV s^{-1}, a slight difference in redox parameters was seen between Ni_3C particles and Ni nanoparticles (NPs) (Table S1). Further, a continuous potential shift of the redox peaks was associated to the formation and diffusion of NiOOH species. From this data the surface coverage of Ni^{2+}/Ni^{3+} redox species (Γ*) could be calculated (see Figures S6cd and S7a and calculations for details).[19] Figure **2 c** compares the coverage of redox species in different KOH concentrations for 0.1 M, 0.5 M and 1.0 M KOH. Considering that the proton diffusion governs the $Ni^{2+} \leftrightarrow Ni^{3+}$ redox reaction process, its diffusion coefficient (*D*) was determined by the *Randles-Sevcik* equation (see Figures S6ef and S7b and calculations).[34] The proton diffusion coefficients obtained in Ni_3C, up to 5.99×10^{-9} cm^2 s^{-1} in 1.0 M KOH (Figure **2 c**), were well above to the values measured for pure Ni NPs.[14] This value indicated the N_3C structure to facilitate

the Ni^{2+}/Ni^{3+} redox process at the basis of the high electrocatalytic activity of Ni-based catalysts. The larger *D* value was ascribed to the lower onset potential, leaving larger potential window (the same applied potential below OER region) for MOR in 1.0 M KOH (Figure **2 a**).[35]

Once methanol was added to the electrolyte, a sharp current density increase associated to the MOR was measured at potentials above 0.35 V, which matched well with the $Ni(OH)_2 \rightarrow NiOOH$ oxidation event (Figures **2 a** and **3 a**). As expected, current densities increased with the KOH concentration, but also with the size and branching of the NPs (Figure **2 a**). The MOR current density on CVs in Ni_3C-based electrodes increased drastically and steadily with increasing methanol concentration up to 0.4 M (Figure **3 b**). To compare the MOR activity with reference materials, the oxidation current was normalized by the surface area or the Ni_3C mass loading. The current density at 0.6 V in 1.0 M KOH and 1.0 M methanol reached 127 mA cm^{-2} and 4.2 A mg^{-1} (averaged from 5 separate electrodes with 10 % error). These activities clearly stand out from previously reported noble metal-free MOR catalysts (Table S2). Discarding a bifunctional and a stearic effect of the carbon within the Ni, we associated the excellent catalytic activities obtained from Ni_3C-based catalysts to an electronic effect; the presence of carbon effectively changes the electronic energy levels on the nickel surface, improving the effectiveness of the reaction sites.[36, 37] Besides, we observed the unique branched geometry to booster the MOR activity by simultaneously providing a large electrolyte/electrode interface for methanol and hydroxide interaction with high electrical conductivity avenues for charge transport.

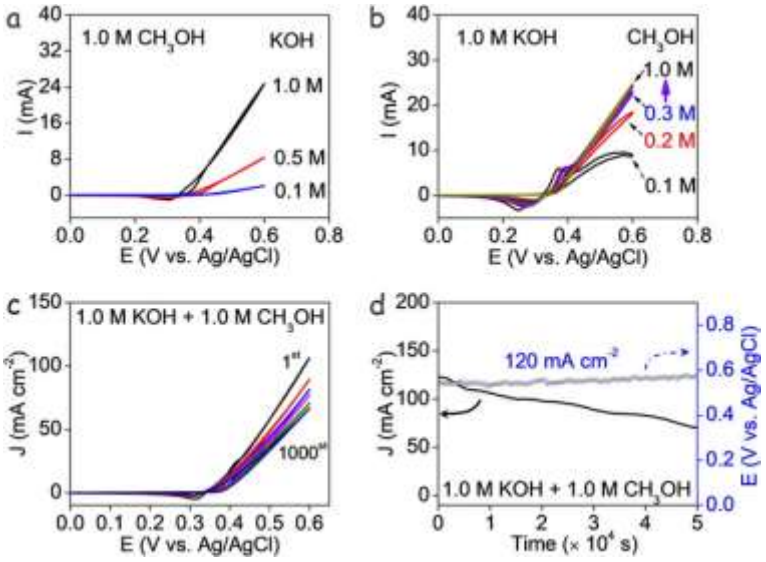

Figure 3. MOR electrochemical performance of Ni_3C-based electrodes. a) CV curves in 0.1, 0.5 and 1.0 M KOH solution with 1.0 M methanol. b) CV curves in 1.0 M KOH with variable methanol concentrations from 0.1 to 1.0 M. c) Continuous CV cycling in the potential range 0–0.6 V with a scan rate of 100 mV s^{-1}. d) CA response at 0.6 V and CP profile at a current density of 120 mA cm^{-2}.

The electrochemical stability of Ni_3C electrocatalysts was evaluated through continuous CV cycling, chronoamperometry (CA) and chronopotentiometry (CP) in 1.0 M KOH containing 1.0 M methanol. Figure **3 c** presents 1000 continuous CV cycles obtained from a branched Ni_3C/C catalyst. The current density at 0.6 V was found to decay 18.1 %, 24.4 %, 28.6 %, and 34.6 % after the 200th, 600th, 800th and 1000th CV, respectively, but maintaining still 69.6 mA cm^{-2} after 1000 cycles. Figure **3 d** shows the CA curve at 0.6 V, where an insignificant OER contribution was measured (Figure **2 a**). In these conditions, as shown in Figure **3 d**, during 50 000 s operation the current density decreased from 125 mA cm^{-2} to 70 mA cm^{-2}, which is still an excellent current density if we compare with initial values reported in previous works (Table S2). As shown in Figure S8, after 50 000 s CA testing the electrocatalyst was characterized by a less branched morphology and a smaller particle size. These changes occurred during the electrocatalytic process in critical alkaline media at high potential.[14, 38-40] Additionally, CP measurements showed that an additional potential of just 0.03 V, above the initial 0.55 V, were required to maintain a current density of 120 mA cm^{-2} for 50 000 s (Figure **3 d**).

To determine the MOR reaction mechanism and the reason behind the excellent catalyst stability, we monitored the MOR activity of Ni_3C-based electrodes using in situ Attenuated Total Reflection Surface-Enhanced Infrared Absorption (ATR-SEIRA) and Infrared Reflection Absorption Spectroscopy (IRAS) in a 0.1 M KOH electrolyte containing 0.5 M methanol. In a homemade spectro-electrochemical cell (Figure **4 a**), catalyst ink was drop-casted on Au. Before the measurement, we excluded the MOR influence of Au (Figure S9). As shown in Figure **4 b**, several IR absorption peaks appeared in the ATR-SEIRA spectra when applying potentials above 0.2 V vs. Ag/AgCl to the Ni_3C electrode. Specifically, IR absorption bands at ca. 2924, 2906 and 2853 cm^{-1} as well as three peaks at 1530, 1450, and 1407 cm^{-1} in the lower wavenumber region are ascribed to surface CH_3O and CH_3OH species (Table S3).[10, 41-44] In addition, the downward bands in the range 1000–1200 cm^{-1} in the raw spectra were associated to the consumption of the methanol during the measurement (Figure S10). Notably, no evidences were found of the presence of neither adsorbed CO species (1700–2000 cm^{-1}) nor of the CO_2 production (2341 cm^{-1}) in the ATR-SEIRA spectra. Nevertheless, the presence of these species cannot be excluded only based on ATR-SEIRA spectra, as weakly-adsorbed or produced species may dissolve into the solution. Thus, we used IRAS to analyze at each electrode potential the dissolved products in a thin electrolyte layer used in this experiment (see setup drawing in Figure **4 c**). As shown in Figure **4 d**, no bands associated with CO and CO_2 could be observed, which excluded the CO-pathway in the MOR on Ni_3C. On the other hand, bands at ca. 1558, 1377 and 1342 cm^{-1} in the IRAS spectra were assigned to formate (Figure **4 e** and Table S3).[41, 45] Note that the peak at 1588 cm^{-1} should be located at ca. 1580 cm^{-1}, but the slight shift observed can be associated to the overlap with the (HOH) band of interfacial water (1630 cm^{-1} downward) present during the

methanol consumption on the particles surface. Additionally, IRAS spectra showed no sign of the presence of CO_2 or carbonate at higher potential, which pointed at formate as the only product of the MOR at the Ni_3C surface. Figure S11 displays the intensity of the band at 1342 cm^{-1} as a function of the applied potential during a typical CV in 0.1 M KOH with 0.5 M methanol. A clear relationship between the current density onset associated to the MOR and the band corresponding to the presence of formate in solution was observed.

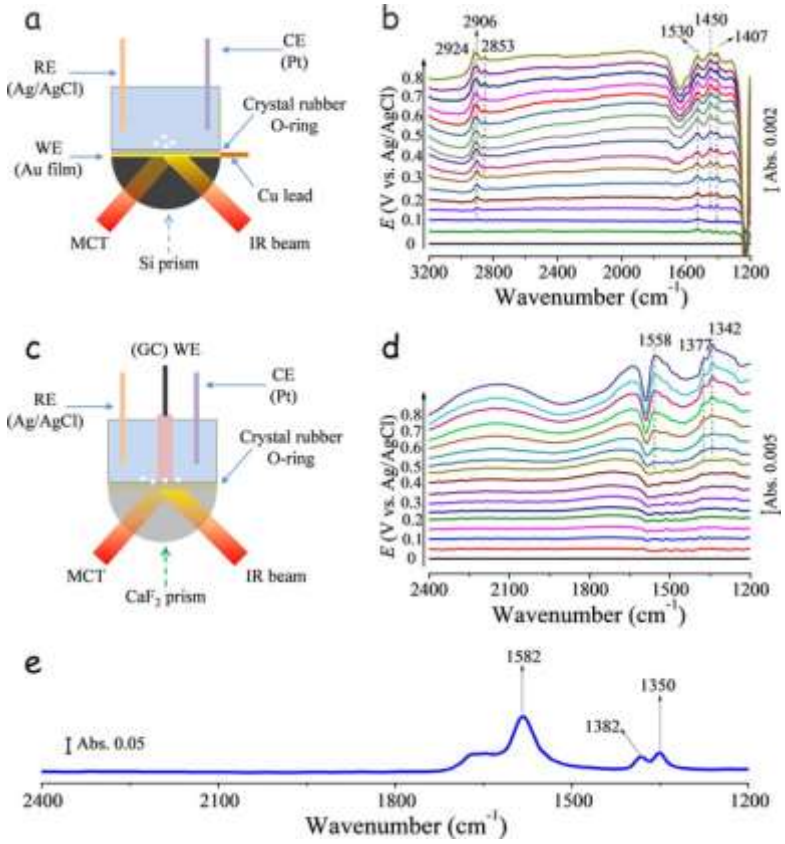

Figure 4. a) Schematic drawing of the ATR-SEIRA set-up. b) Real-time ATR-SEIRA spectra taken on branched Ni_3C surface in 0.1 M KOH and 0.5 M methanol in the potential range 0–0.8 V vs. Ag/AgCl. c) Schematic drawing of a typical setup for IRAS. d) Real-time spectra of MOR on branched Ni_3C particles surface in 0.1 M KOH and 0.5 M methanol in the same potential range 0–0.8 V. e) Transmission spectra of 0.05 M HCOONa and 0.1 M KOH. Note that the single-beam spectrum collected at 0 V was used as the reference spectrum of the real-time spectra, and spectral resolution is 8 cm^{-1}.

To validate our results, an aliquot of the electrolyte after MOR operation in 1.0 M KOH + 1.0 M methanol was analyzed by NMR (Figure S12). ^{13}C NMR analysis indicated that the formate was the only product after 50 000 s reaction, further demonstrating the highly selective conversion of methanol to formate over Ni_3C catalysts in alkaline media.

In summary, we presented a new MOR catalyst based on abundant elements able to selectively and effectively convert methanol-to-formate. Electrochemical measurements combined with advanced in situ infrared spectroscopy and NMR analysis allowed to clearly determine the reaction products ruling out the adsorption of CO and the production of carbonates. This highly selective conversion on Ni_3C electrodes exhibited a remarkable current density of 127 mA cm^{-2}, corresponding to 4.2 A mg^{-1} at 0.6 V vs. Ag/AgCl in 1.0 M KOH containing 1.0 M methanol. This work offers the first evidence for this selective methanol-to-formate conversion in Ni-based non-noble catalysts and provides a very promising example to exploit non-precious metal electrocatalysts for the electrocatalytic conversion of small organic molecules.

Acknowledgements

J. Li obtained an International Postdoctoral Exchange Fellowship Program (Talent-Introduction program) in 2019 and is grateful for the project (2019M663468) funded by the China Postdoctoral Science Foundation. This work was supported from the UESTC start-up funding and the Recruitment Program of Thousand Youth Talents. Y. Yang acknowledges the funding No.21603177 from NSFC. It was also supported by the European Regional Development Funds and by the Spanish Ministerio de Economía y Competitividad through the project SEHTOP (ENE2016-77798-C4-3-R) and VALPEC (ENE2017-85087-C3). X. Wang, Y. Zuo, and X. Han thank the China Scholarship Council (CSC) for scholarship support. X. Han and J. Arbiol acknowledge funding from Generalitat de Catalunya 2017 SGR 327. ICN2 acknowledges support from the Severo Ochoa Programme (MINECO, Grant no. SEV-2013-0295). IREC and ICN2 are funded by the CERCA Programme/Generalitat de Catalunya. Part of the present work has been performed in the framework of Universitat Autònoma de Barcelona Materials Science PhD program. J. Llorca is a Serra Húnter Fellow and is grateful to MICINN/FEDER RTI2018-093996-B-C31, GC 2017 SGR 128 and to ICREA Academia program.

Conflict of interest

The authors declare no conflict of interest.

References

1 A. Sartbaeva, V. L. Kuznetsov, S. A. Wells, P. P. Edwards, Energy Environ. Sci. 2008, 1, 79– 85.

2 N. Kakati, J. Maiti, S. H. Lee, S. H. Jee, B. Viswanathan, Y. S. Yoon, Chem. Rev. 2014, 114, 12397– 12429.

3 S. P. S. Badwal, S. Giddey, A. Kulkarni, J. Goel, S. Basu, Appl. Energy 2015, 145, 80– 103.

4 X. Zhao, M. Yin, L. Ma, L. Liang, C. Liu, J. Liao, T. Lu, W. Xing, Energy Environ. Sci. 2011, 4, 2736.

5 E. Herrero, W. Chrzanowski, A. Wieckowski, J. Phys. Chem. 1995, 99, 10423– 10424.

6 H. Robles, Encyclopedia of Toxicology, Wiley-VCH, Weinheim, 2005, pp. 378– 380.

7 Q. Liu, L. Wu, S. Gülak, N. Rockstroh, R. Jackstell, M. Beller, Angew. Chem. Int. Ed. 2014, 53, 7085– 7088;

8 M. Li, X. Deng, K. Xiang, Y. Liang, B. Zhao, J. Hao, J. L. Luo, X. Z. Fu, ChemSusChem 2020, 13, 914– 921.

9 J. Eppinger, K. W. Huang, ACS Energy Lett. 2017, 2, 188– 195.

10 Y. Y. Yang, J. Ren, H. X. Zhang, Z. Y. Zhou, S. G. Sun, W. B Cai, Langmuir 2013, 29, 1709– 1716.

11 W. Huang, H. Wang, J. Zhou, J. Wang, P. N. Duchesne, D. Muir, P. Zhang, N. Han, F. Zhao, M. Zeng, J. Zhong, C. Jin, Y. Li, S. T. Lee, H. Dai, Nat. Commun. 2015, 6, 10035.

12 S. Das, K. Dutta, P. P. Kundu, J. Mater. Chem. A 2015, 3, 11349– 11357.

13 H. Sun, Y. Ye, J. Liu, Z. Tian, Y. Cai, P. Li, C. Liang, Chem. Commun. 2018, 54, 1563– 1566.

14 J. Li, Y. Zuo, J. Liu, X. Wang, X. Yu, R. Du, T. Zhang, M. F. Infante-Carrió, P. Tang, J. Arbiol, J. Llorca, Z. Luo, A. Cabot, J. Mater. Chem. A 2019, 7, 22036– 22043.

15 H. Liu, C. Song, L. Zhang, J. Zhang, H. Wang, D. P. Wilkinson, J. Power Sources 2006, 155, 95–110.

16 J. Wang, D. Teschner, Y. Yao, X. Huang, M. Willinger, L. Shao, R. Schlögl, J. Mater. Chem. A 2017, 5, 9946– 9951.

17 S. Rezaee, S. Shahrokhian, Appl. Catal. B 2019, 244, 802– 813.

18 J. Li, Z. Luo, Y. Zuo, J. Liu, T. Zhang, P. Tang, J. Arbiol, J. Llorca, A. Cabot, Appl. Catal. B 2018, 234, 10– 18.

19 X. Cui, P. Xiao, J. Wang, M. Zhou, W. Guo, Y. Yang, Y. He, Z. Wang, Y. Yang, Y. Zhang, Z. Lin, Angew. Chem. Int. Ed. 2017, 56, 4488– 4493;

20 C. C. L. McCrory, S. Jung, J. C. Peters, T. F. Jaramillo, J. Am. Chem. Soc. 2013, 135, 16977–16987.

21 S. L. Candelaria, N. M. Bedford, T. J. Woehl, N. S. Rentz, A. R. Showalter, S. Pylypenko, B. A. Bunker, S. Lee, B. Reinhart, Y. Ren, S. P. Ertem, E. B. Coughlin, N. A. Sather, J. L. Horan, A. M. Herring, L. F. Greenlee, ACS Catal. 2017, 7, 365– 379.

22 A. A. Dubale, Y. Zheng, H. Wang, R. Hübner, Y. Li, J. Yang, J. Zhang, N. K. Sethi, L. He, Z. Zheng, W. Liu, Angew. Chem. Int. Ed. 2020, 59, 13891– 13899;

23 J. Li, Z. Luo, F. He, Y. Zuo, C. Zhang, J. Liu, R. Du, X. Yu, T. Zhang, P. Tang, M. F. I. Carrió, J. Arbiol, J. Llorca, A. Cabot, J. Mater. Chem. A 2018, 6, 22915– 22924.

24 Y. Y. Tong, C. D. Gu, J. L. Zhang, M. L. Huang, H. Tang, X. L. Wang, J. P. Tu, J. Mater. Chem. A 2015, 3, 4669– 4678.

25 Q. Luo, M. Peng, X. Sun, A. M. Asiri, RSC Adv. 2015, 5, 87051– 87054.

26 M. Mazloum-Ardakani, V. Eslami, A. Khoshroo, Mater. Sci. Eng. B 2018, 229, 201– 205.

27 Z. L. Schaefer, K. M. Weeber, R. Misra, P. Schiffer, R. E. Schaak, Chem. Mater. 2011, 23, 2475– 2480.

28 L. Qiao, W. Zhao, Y. Qin, M. T. Swihart, Angew. Chem. Int. Ed. 2016, 55, 8023– 8026;

29 J. F. Moulder, W. F. Stickle, P. E. Sobol, K. D. Bomben, Handbook of X-Ray Photoelectron Spectroscopy, PerkinElmer Corporation Physical Electronics Division, 1979, p. 81.

30 J. Li, X. Xu, Z. Luo, C. Zhang, Y. Zuo, T. Zhang, P. Tang, M. F. Infante-Carrió, J. Arbiol, J. Llorca, J. Liu, A. Cabot, ChemSusChem 2019, 12, 1451– 1458.

31 J. Li, X. Xu, X. Yu, X. Han, T. Zhang, Y. Zuo, C. Zhang, D. Yang, X. Wang, Z. Luo, J. Arbiol, J. Llorca, J. Liu, A. Cabot, ACS Appl. Mater. Interfaces 2020, 12, 4414– 4422.

32 J. D. Benck, Z. Chen, L. Y. Kuritzky, A. J. Forman, T. F. Jaramillo, ACS Catal. 2012, 2, 1916– 1923.

33 C. C. L. McCrory, S. Jung, I. M. Ferrer, S. M. Chatman, J. C. Peters, T. F. Jaramillo, J. Am. Chem. Soc. 2015, 137, 4347– 4357.

34 A. J. Bard, L. R. Faulkner, Electrochemical Methods: Fundamentals and Applications, Wiley, New York, 2001.

35 S. J. Zhang, Y. X. Zheng, L. S. Yuan, L. H. Zhao, J. Power Sources 2014, 247, 428– 436.

36 A. Sadiki, P. Vo, S. Hu, T. S. Copenhaver, L. Scudiero, S. Ha, J. L. Haan, Electrochim. Acta 2014, 139, 302– 307.

37 M. Wang, X. Zhang, H. Li, J. Lu, M. Liu, F. Wang, ACS Catal. 2018, 8, 1614– 1620.

38 C. Cui, L. Gan, M. Heggen, S. Rudi, P. Strasser, Nat. Mater. 2013, 12, 765– 771.

39 Y. Zuo, Y. Liu, J. Li, R. Du, X. Han, T. Zhang, J. Arbiol, N. J. Divins, J. Llorca, N. Guijarro, K. Sivula, A. Cabot, Chem. Mater. 2019, 31, 7732– 7743.

40 X. Yu, Z. Luo, T. Zhang, P. Tang, J. Li, X. Wang, J. Llorca, J. Arbiol, J. Liu, A. Cabot, Chem. Mater. 2020, 32, 2044– 2052.

41 S. E. Collins, M. A. Baltanás, A. L. Bonivardi, Appl. Catal. A 2005, 295, 126– 133.

42 Y. Liu, M. Muraoka, S. Mitsushima, K. I. Ota, N. Kamiya, Electrochim. Acta 2007, 52, 5781– 5788.

43 A. Zalineeva, S. Baranton, C. Coutanceau, Electrochim. Acta 2015, 176, 705– 717.

44 Y. Zhu, H. Uchida, T. Yajima, M. Watanabe, Langmuir 2001, 17, 146– 154.

45 A. Kowal, S. N. Port, R. J. Nichols, Catal. Today 1997, 38, 483– 492.